Elsevier Editorial System(tm) for Earth and Planetary Science Letters

Manuscript Draft

Manuscript Number:

Title: Electrolytic Fluid Speciation by Gibbs Energy Minimization and Implications for Subduction Zone Mass Transfer

Article Type: Letters

Keywords: Electrolytic fluid speciation; Gibbs energy minimization; subduction; devolatilization; mass transfer; decarbonation

Corresponding Author: Dr. James A.D. Connolly,

Corresponding Author's Institution:

First Author: James A.D. Connolly

Order of Authors: James A.D. Connolly

Abstract: The number of solute species required to describe the thermodynamic behavior of electrolytic fluids is a hindrance to the incorporation of aqueous geochemistry in petrological Gibbs energy minimization procedures. An algorithm is developed to overcome this problem. Beginning from the solute-free limit, chemical potentials and phase stability are determined by minimization, the solute speciation and bulk fluid properties consistent with these chemical potentials are then computed and the procedure repeated until the chemical potentials converge. Application of the algorithm to a model for metamorphism of subduction sediment shows that accounting for solute chemistry does not change the conclusion based on molecular fluid models that a pervasive water flux from the subjacent mantle is required to explain island-arc CO2 emissions by fluid-mediated slab decarbonation. This putative flux would deplete the sediment in potassium, rendering the slab refractory to melting and limiting its capacity to transport water to greater depth.

Suggested Reviewers: Maria Frezzotti
maria.frezzotti@unimib.it

Craig Manning
manning@epss.ucla.edu

Dimitri Sverjensky
sver@jhu.edu

simone tumiati
simone.tumiati@unimi.it

mark ghiorso
ghiorso@ofm-research.org

Opposed Reviewers:

Eidgenössische Technische Hochschule Zürich
Swiss Federal Institute of Technology Zurich

Institut für Geochemie und Petrologie

ETH Zentrum
CH-8092 Zürich

Tel. +41-44-632 78 04
Fax +41-44-632 16 36
james.connolly@erdw.ethz.ch

April 13, 2018

Dear EPSL:

Herewith please find a manuscript on a method for incorporating electrolytic fluid speciation in Gibbs energy minimization calculations and its application to subduction zone mass transfer that I submit for your consideration as a publication in EPSL.

It is difficult to place this work fairly in scientific context because existing Gibbs energy minimization codes (e.g., Harvie et al. 1987; Karpov et al., 2001) already have the capability to treat electrolytic fluids robustly. The limitations of the existing codes are practical rather than algorithmic. In contrast, the algorithm developed and implemented in this paper is imperfect, but it makes practical a broad spectrum of geochemical problems that are not currently tractable. Rather than bore the reader with lists of technicalities about what program X can do, but program Y cannot do, I have demonstrated the capabilities of the method through an application to subduction zone mass transfer.

The thermodynamic data necessary for the application to subduction zones is highly uncertain, but I believe the results have scientific value. Specifically, these results suggest that: 1) solute chemistry increases carbon solubility in subduction zone fluids by roughly a factor of two; 2) fluid-mediated decarbonation of subducted oceanic crust requires water infiltration from an external source; 3) that such an infiltration event would have profound geochemical consequences, notably K depletion; and 4) that subducted sulfides become soluble by the reduction of carbonate to produce diamond.

Sincerely,

James A. D. Connolly

***Highlights (for review)**

Highlights:

- Electrolytic fluid speciation is implemented in a Gibbs energy minimization code.
- Dissolution increases C-solubility two-fold compared to molecular fluid models.
- Infiltration-driven decarbonation desiccates the crust by K-depletion.
- Sulfides become soluble by the reduction of carbonate to diamond at ~6 GPa.

*Manuscript
Click here to view linked References

Electrolytic Fluid Speciation by Gibbs Energy Minimization and Implications for Subduction Zone Mass Transfer

James A. D. Connolly (james.connolly@erdw.ethz.ch)
Department of Earth Sciences
Swiss Federal Institute of Technology
CH-8092 Zurich

Abstract

The number of solute species required to describe the thermodynamic behavior of electrolytic fluids is a hindrance to the incorporation of aqueous geochemistry in petrological Gibbs energy minimization procedures. An algorithm is developed to overcome this problem. Beginning from the solute-free limit, chemical potentials and phase stability are determined by minimization, the solute speciation and bulk fluid properties consistent with these chemical potentials are then computed and the procedure repeated until the chemical potentials converge. Application of the algorithm to a model for metamorphism of subduction sediment shows that accounting for solute chemistry does not change the conclusion based on molecular fluid models that a pervasive water flux from the subjacent mantle is required to explain island-arc CO_2 emissions by fluid-mediated slab decarbonation. This putative flux would deplete the sediment in potassium, rendering the slab refractory to melting and limiting its capacity to transport water to greater depth.

Keywords: Electrolytic fluid speciation, Gibbs energy minimization, subduction, devolatilization, mass transfer, decarbonation.

1. Introduction

Gibbs energy minimization is applied to a broad spectrum of geochemical and petrological problems (Leal et al., 2017). In geochemistry the focus of these applications is usually modelling reactive transport (Wolery, 1992; Bethke, 1996), whereas in petrology the focus is predicting phase stability (DeCapitani and Brown, 1987; Connolly, 2009). This disparity has led to a situation in which geochemical codes account for complex fluid chemistry, but often seek only a local equilibrium solution, whereas petrologic codes seek a costly global solution that limits their ability to treat the complex fluid chemistry. As a means of bridging this gap Galvez et al. (2015; Galvez et al., 2016) use phase equilibria computed by Gibbs energy minimization assuming a solute-free fluid to back-calculate solute chemistry. This method accurately estimates solute chemistry provided the solute mass is small compared to the total mass of the system, but is not well suited for reactive transport problems because the phase proportions and bulk fluid chemistry are not rigorously determined. The present work improves on this method by incorporating back-calculated fluid chemistry in an iterative Gibbs energy minimization procedure referred to here as lagged speciation.

The utility of the lagged speciation algorithm is demonstrated by a model for devolatilization of subduction zone sediments. This problem has been made tractable by the Deep Earth Water (DEW) model for electrolytic fluids (Sverjensky et al., 2014), which extends the Helgeson-Kirkham-Flowers (HKF) formulation (Shock and Helgeson, 1988) for aqueous species to high pressure conditions. Although a number of studies have considered the implications of the DEW model for fluid-dominated subduction zone chemistry (Facq et al., 2014; Sverjensky and Huang, 2015; Tumiati et al., 2017), the present focus is the rock-dominated limit appropriate in systems where the fluid is generated by devolatilization. This limit was investigated by Galvez et al. (2015) using a variant of the DEW model. The distinction between the DEW model and the

Galvez et al. (2015) variant, is that in the DEW model the solvent is H_2O and molecular volatiles are treated as solute species, whereas in Galvez et al. (2015) the solvent is a mixture of molecular volatiles. Both approaches are compared.

Subduction zone devolatilization is topical because of its potential role in various global element cycles. The observation, based on simple sub-solidus phase equilibrium models (Kerrick and Connolly, 2001ab) that carbonates persist within subducted slabs beyond sub-arc depth has motivated alternative hypotheses to explain extensive slab decarbonation and/or island-arc emissions. These hypotheses include: infiltration-driven decarbonation (Connolly 2005; Gorman et al., 2006); carbon transfer by entrainment or diapirism (Dasgupta et al., 2004; Behn et al., 2011); slab-melting (Poli, 2015; Skora et al., 2015); or near-surface provenance volcanic CO_2 (Mason et al., 2017). With the exception of the latter, all of these mechanisms are viable but unsatisfying in that they require a coincidence of processes or extreme temperatures. Evidence of subsolidus carbonate dissolution (Frezzotti et al., 2011; Ague and Nicolescu, 2014) has prompted the suggestion that, by neglecting the solubility of non-volatile elements, early models underestimated the efficacy of simple decarbonation processes. Previous work (Kelemen and Manning 2015; Galvez et al., 2015) suggests that at typical subduction zone conditions dissolution causes a two-fold increase in the carbon content of subduction zone fluids, but does not address fluid production. The models here extend that work by tracking fluid evolution from the surface to beyond sub-arc depths.

This paper begins with a generalization of the back-calculation method (Galvez et al., 2015). The lagged speciation algorithm by which back-calculated results may be integrated into a Gibbs energy minimization procedure is then outlined and the limitations of the algorithm are explained. The final major section uses the subduction zone model to illustrate some

technicalities of the method and to explore the consequences of solute chemistry on closed, open, and infiltration-driven devolatilization scenarios.

2. Back-Calculated Speciation

Back-calculated speciation designates the calculation of the solute speciation of an electrolytic fluid under the assumptions of charge balance, equilibrium, known solvent composition, and specified chemical potentials. The partial molar Gibbs energy of any species can be expressed as

$$g^i = -n^i_{e^-}\mu_{e^-} + \sum_{j=1}^{c} n^i_j \mu_j \qquad 1$$

where c is the number of components, μ_i and μ_{e^-} are, respectively, the chemical potential of component j and the electron, and for species i: n^i_j is the molar amount of component j and $-n^i_{e^-}$ is the molar charge, abbreviated hereafter q^i. Equation 1 can be rearranged to express μ_{e^-} in terms of the chemical potentials and the properties of charged species i

$$\mu_{e^-} = \frac{1}{q^i}\left(g^i - \sum_{j=1}^{c} n^i_j \mu_j \right). \qquad 2$$

Because μ_{e^-} is the same for all species at equilibrium, equating the right-hand-side of Equation 2 for two distinct charged species yields a relation between the partial molar Gibbs energy of any arbitrarily chosen charged species and the partial molar Gibbs energy of a charged reference species k

$$g^i = \frac{q^k}{q^i}\left(g^k + \sum_{j=1}^{c} \mu_j \Delta n^i_j \right) \qquad 3$$

where $\Delta n^i_j = n^k_j - n^i_j$. In terms of a solute reference state activity model, the partial molar Gibbs energies in Equation 3 are

$$g^i = g^{*,i} + \mathrm{R}T \ln\left(m^i \gamma^i \right) \qquad 4$$

where $g^{*,i}$ is the solute reference state molar Gibbs energy; m^i is the molal concentration, γ^i is the activity coefficient, T is temperature, and R is the universal gas constant. Substituting Equation 4 into Equation 3 and rearranging the result

$$m^i = \frac{c^i}{\gamma^i}\left(m^k\gamma^k\right)^{q^k/q^i} \qquad 5$$

where

$$c^i = \exp\left(\frac{q^k}{q^i}\left[g^{*,k} + \sum_{j=1}^{c}\mu_j\Delta n_j^i\right] - g^{*,i}\Big/RT\right).$$

Substituting Equation 5 into the charge balance constraint for a fluid with s charged solute species

$$\sum_{i=1}^{s} q^i m^i = 0 \qquad 6$$

yields

$$\sum_{i=1}^{s}\frac{q^i c^i}{\gamma^i}\left(m^k\gamma^k\right)^{q^k/q^i} = 0\,, \qquad 7$$

which can be solved in the ideal limit ($\gamma^i \to 1$) for m^k if the composition of the solvent, which influences $g^{*,i}$, is known. The concentrations of the remaining charged species are then obtained from Equation 5 and those of neutral species from Equation 4. In the non-ideal case, additional assumptions are necessary to compute the activity coefficients. Regardless of those details, the flaw in this method is that if the solvent composition is consistent with the specified chemical potentials, as is the case when the chemical potentials and solvent composition are obtained by Gibbs energy minimization, then finite solute concentrations violate this consistency. This flaw has the consequence that, except in the limit of infinite dilution ($m^i \to 0$), there is no bulk fluid composition that simultaneously satisfies Equation 7 and the constraint on the chemical potentials of the system.

3. The Lagged Speciation Algorithm

The limitation of simple back-calculated speciation is the absence of a relation between the calculated solute chemistry and the bulk chemistry of the fluid, which precludes evaluation of mass balance constraints. To circumvent this limitation, the present work exploits the iterative aspect of Gibbs energy minimization by successive linear programming (Connolly 2009). The essential feature of successive linear programming is that an initial result in which the compositions of the phases are discretized at some specified resolution is iteratively refined until a desired target resolution has been achieved. The innovation here is to use a minor modification of the back-calculated speciation algorithm to estimate the Gibbs energy and composition of the stable fluid(s). In the initial optimization, the fluid may contain multiple solvent species (e.g., H_2O, CO_2, CH_4, H_2S), but is solute-free. Given the solute-free solvent composition(s) and chemical potentials obtained in this optimization, the reference state solute partial molar Gibbs energies are computed, Equation 7 is solved for the concentration of the reference ion, and Equations 4 and 5 are solved for the concentrations of the remaining solute species. The solvent mole fractions are then recomputed as

$$y^i_{h+1} = \frac{m^i_h}{m_{total}} \quad i = s+1,\ldots,r \tag{8}$$

with

$$m_{total} = \sum_{i=1}^{s} m^i_h + \sum_{i=s+1}^{r} y^i_h \quad . \tag{9}$$

where r is the number of solvent species, h indexes the iteration level. The Gibbs energy and bulk composition for the fluid used in the succeeding iteration are

$$g_{h+1} = \sum_{i=1}^{s}\left(m^i_h\left[g^{*,i} + \mathrm{R}T\ln\left(m^i_h\gamma^i_h\right)\right]\right) + \sum_{i=s+1}^{r}\left(m^i_h\left[g^{0,i} + \mathrm{R}T\ln\left(y^i_{h+1}\gamma^i_{0,h}\right)\right]\right) \tag{10}$$

$$n_{j,h+1} = \sum_{i=1}^{s} m^i_h n^i_j + \sum_{i=s+1}^{r} m^i_{h+1} n^i_j \quad j = 1,\ldots,c\ . \tag{11}$$

where $\gamma^i_{0,h}$ is the activity coefficient of solvent species *i* in the solute-free solvent. Equation 10 ignores the dependence of the solvent species activity coefficients on solute concentration and is therefore thermodynamically consistent only in the ideal limit (e.g., Wolery 1990). Although it is not algorithmically required, the inconsistent form is maintained because electrolytic fluid species activity models are currently poorly constrained. In contrast, molecular fluid equations of state are capable of predicting species activities in the solute-free solvent with good accuracy (Prausnitz, 1969). Excepting this inconsistency, and in contrast to simple back-calculation, iterative application of Equation 10 reaches a thermodynamically consistent solution provided the lagged chemical potentials, used to compute the solute molalities m^i_h by back-calculation, converge.

3.1 Algorithmic Limitations

Because the lagged speciation algorithm predicts fluid composition from a back-calculated result convergence to a stable solution is not guaranteed. The condition for algorithmic failure is that no combination of phases involving the solute-bearing fluid simultaneously satisfy mass balance and minimize the Gibbs energy of the system. This condition may be manifest in two distinct ways which are outlined in detail below because the ability to recognize failure is essential for the practical implementation of an imperfect algorithm.

The more easily understood manifestation of algorithmic failure is illustrated schematically for the H_2O-SiO_2 system at conditions where, depending on bulk composition, the stable phase assemblages are quartz (q) + fluid (F) or fluid (Fig 1). For any general composition, the initial, solute-free, optimization identifies q + pure-water (H_2O) as the stable phase assemblage. Simple back-calculation from this result corresponds to a Gibbs-energy composition coordinate (blue, Fig 1a) on the line connecting the coordinates of quartz and pure-water, whereas the coordinate computed by lagged speciation (Eqs 8 and 9) must lie below this line, at least in the

ideal limit. If the bulk composition of the system is more silica-rich than the fluid the iteration proceeds stably because the assemblage q + F provides a physically meaningful basis for estimating the chemical potentials of the system. However, if the bulk composition lies on the water-rich side of the fluid composition, the successive optimization will identify F + H_2O as the stable phase assemblage. This assemblage does not correspond to a real phase assemblage and therefore provides no basis for refining the chemical potentials of the system in the subsequent iteration. A more insidious problem is that the chemical potential of H_2O for this pseudo-phase assemblage must be equal to the partial molar Gibbs energy of pure water. Thus, the fluid speciation obtained by back-calculation recovers the simple back-calculated result and subsequent iterations will oscillate between these solutions. The condition for algorithmic stability deduced from this behavior is that if an element is represented in the fluid only by solute species, then this element must be present in at least one stable phase other than the fluid. For example, if K dissolves in the fluid only as a solute species, the lagged speciation algorithm will fail when K is dissolved entirely in the fluid.

In systems with more than one solute-component algorithmic failure can be manifest in an additional way that is illustrated schematically for the H_2O-$CaSiO_3$-SiO_2 system at a condition at such that wollastonite (wo) + quartz stably coexist (Fig 2a). Assuming Ca and Si can be present in the fluid only as solute species, then, for any general composition, the initial optimization will identify wollastonite + quartz + H_2O as the stable phase field. Lagged speciation then identifies the composition of the fluid that coexists with wollastonite + quartz (F in Fig 2b), and in the next iteration there, from the algorithmic perspective, three prospective phase fields: wo + q + F; wo + H_2O + F; and q + H_2O + F. The latter two fields do not correspond to real phase assemblages and provide no basis for refining the chemical potentials of the system. Thus, the iteration scheme becomes unstable if the systems composition lies within these fields.

Both of the preceding examples illustrate the rock-dominated limit of Galvez et al. (2015). Formally, in simple back-calculation the only robust formulation of this limit is that solute concentrations are negligible. As such the limit is unduly restrictive and has little practical utility other than to indicate that back-calculation is likely to be accurate if the fluid mass is small. The utility of incorporating back-calculated speciation in a Gibbs energy minimization procedure, is that the minimization procedure automatically evaluates mass balance constraints and thereby quantitatively determines the rock-dominated limit. Within this limit, the lagged-speciation algorithm is unconditionally stable.

4. Devolatilization of Subduction Zone Sediment

To provide a minimal, but representative, model for subduction zone devolatilization the geotherm (Fig 3) adopted here represents subduction of a young (40 Ma) slab at a rate of 10 cm/y and a kinematically prescribed dip of 45° (Rupke et al., 2004). The age and rate differ slightly from the global mean (~55 Ma and ~6 cm/y) and the dip is roughly the median of observed slab dips (Stern, 2002). Sediment lithologies are heterogeneous, rather than consider this compositional spectrum, the global average marine sediment (GLOSS, Plank and Langmuir, 1998) composition is adopted as being representative (Table 1). Previous phase equilibrium modeling (Kerrick and Connolly, 2001a) indicates that the high water content of the GLOSS composition favors decarbonation at low temperature compared to water-poor carbonate sediments and as such provides a best case scenario for sub-arc decarbonation. Because the GLOSS average does not quantify the redox state of iron or carbon, the initial bulk oxygen content is computed under the assumption that all iron is ferrous and all carbon is present as carbonate, a configuration identified here as the neutral bulk redox state. In the resulting models, the stability of ferric iron in low-temperature minerals has the consequence that a small amount of carbonate is reduced to form graphite at surface conditions and graphite or diamond persists, except in the infiltration model, as a stable phase at all conditions.

Preliminary calculations demonstrated that an implausible initial ferric/ferrous ratio of ~2.5 would be necessary to completely suppress the stability of reduced carbon during devolatilization. At the opposite extreme, essentially all the initial carbon must be reduced to destabilize carbonate. This extreme leads to dramatically different devolatilization behavior in that at low pressures (< ~1.5 GPa) almost all carbon is released in the form of a methane-rich fluid, an effect that may be of some interest but effectively eliminates decarbonation as a mechanism for explaining island-arc decarbonation. These considerations suggest that predictions based on the neutral bulk redox state initial condition are likely to be characteristic of natural conditions and, to a first approximation, account for the presence of organic carbon in marine sediments (Bebout, 1995).

Sulfur is an important, but oft neglected, component of subduction zone volatile budgets (Pokrovski and Dubrovinsky, 2011; Evans et al., 2014; Kagoshima et al., 2015; Canil and Fellows, 2017). To evaluate the effect of Sulfur, the GLOSS composition (Table 1) was modified by the addition of 0.1 mol S_2/kg. The sulfur is presumed to be accommodated in pyrite (~0.6 vol %) and the bulk oxygen content reduced accordingly, i.e., the bulk molar O_2 content is reduced by half the molar S_2 content. The possibility of the presence of oxidized sulfur in the initial bulk composition was not considered because in preliminary calculations sulfates were not predicted to coexist with graphite + carbonate at surface conditions.

The DEW/HKF data base (Shock and Helgeson, 1988; Sverjensky et al., 2014) includes 28 C-O-H-S solute species. In initial calculations the concentrations of glycolate ($C_2H_3O_3^-$), glutarate ($C_5H_7O_4^-$), and lactate ($C_3H_5O_3^-$) were implausibly high at all conditions of interest. Accordingly, these species were not considered in the H_2O-solvent model calculations. In mixed-volatile solvent calculations (the COHS-solvent model), none of the DEW/HKF C-O-H-S solute species were considered, and the solvent was initially treated as a mixture of H_2O, H_2, CO, CO_2, CH_4, SO_2, and H_2S species. These calculations demonstrated that H_2, CO_2, CH_4, SO_2, and H_2S had

no significant effect on solute speciation or bulk chemistry. The final calculations considered only the four dominant species (H_2O, CO_2, CH_4, and H_2S).

Results are presented for closed system sediment devolatilization computed by lagged speciation with the COHS-solvent model. These results are compared to four variants to illustrate technical differences and to inform the devolatilization process. Specifically, the variants, and their purposes, are: 1) simple back-calculation, to contrast the lagged- and back-calculation methods; 2) H_2O-solvent, to illustrate the consequences of the choice of solvent model on fluid speciation and chemistry; 3) fluid-fractionation, a more realistic open-system model for devolatilization; and 4) infiltration-driven devolatilization, an effective, if poorly constrained, mechanism for slab-decarbonation.

Thermodynamic details of the model calculations and the implementation of the DEW/HKF formulation are summarized in the Appendix. The computer program and data files used for these calculations are available at www.perplex.ethz.ch.

4.1 Devolatilization vs Dissolution

The difference between the phase proportions predicted for GLOSS subduction models that account for both devolatilization and dissolution (Fig 4a) as opposed to a model without dissolution (Fig 4b) is surprisingly large. Most notably in the absence of dissolution white mica undergoes no significant dehydration. In contrast, in the lagged speciation model, mica is almost completely dehydrated at the maximum pressure, 6.6 GPa, of the profile. Likewise, without dissolution, the proportions of pyrite and aragonite are approximately constant after dolomite is destabilized at ~5 GPa, but in the lagged speciation model pyrite and aragonite are eliminated by dissolution at 6.4 GPa. The maximum pressure at which phase relations are computed in the

lagged-speciation calculation is the point at which the fluid composition becomes so solute-rich that the rock-dominated limit (Fig 2) is violated.

Although not easily visible (Fig 4b), the volume of diamond increases ten-fold, to ~0.1%, over the same interval that aragonite begins to dissolve. From the fluid speciation (Fig 5a), it is apparent that this phase of diamond precipitation is related to an increase in the concentration of $CaSO_4$ in the fluid, which forms by the reduction of carbon bound in aragonite. This prediction is consistent with the observation of sulfate species and solid carbonate in fluid inclusions in natural subduction zone diamonds (Frezzotti et al., 2011). In calculations not reproduced here, Aragonite and mica are destabilized at essentially the same conditions for the S-free GLOSS composition; therefore, this process is not dependent on the stability of aqueous $CaSO_4$ and the oxidation of pyrite.

As anticipated by earlier studies (Manning et al., 2013; Galvez et al., 2015), dissolution roughly doubles carbon loss (Fig 6a). In early models of slab-decarbonation (Kerrick and Connolly, 2001ab), closed system results were used to estimate carbon transfer under the assumption that the accumulated fluid is released in a single batch at sub-arc depth. On a global scale the fluid-mediated mass transfer of element *i* is

$$Q_i = v_s h_0 \rho_0 N_i n_i \qquad (12)$$

where v_s is the global subduction rate (2.7 km^2/y, Stern, 2002), h_0 and ρ_0 are initial thickness and density of the source rock, N_i is the atomic weight, and n_i is the number of moles of element released by a unit mass of the source rock (Fig 6a). For present purposes, it is assumed that the bulk of the slab carbon is contained in a 1300 m thick section consisting of 800 m of GLOSS sediment (Plank and Langmuir, 1998) and 500 m of hydrothermally altered basalt (Staudigel et al., 1989). Both lithologies have comparable initial carbon content (0.7 mol/kg) and density

(2600±100 kg/m^3) in which case the carbon input by subduction of oceanic crust is 76 Mt/y, which lies within the range of recent estimates (35-88 Mt/y; Kerrick and Connolly, 2001a; Dasgupta and Hirschmann, 2010; Kelemen and Manning, 2015). To make a first order assessment of the global carbon-loss, it is assumed that carbon-loss in the basalt section is comparable to that computed for GLOSS sediment. Justification for this assumption follows from the mineralogical similarity of sedimentary and basaltic eclogites (Kelemen and Manning, 2015). Based on these assumptions the global carbon loss for batch devolatilization with (n_C = 0.28 mol/kg, Fig 6a) and without (n_C = 0.12 mol/kg) dissolution is 30.6 Mt/y and 13.1 Gt/y, these values compare with estimates of island-arc carbon emissions (18-55 Mt/y, Kerrick and Connolly, 2001a; Dasgupta and Hirschmann, 2010; Kelemen and Manning, 2015). At face value, this result suggests dissolution resolves the mismatch between predicted carbon loss and the observed carbon emission; however, that conclusion is not justified in light of model uncertainty. For example, an increase of 100 K, which is well within the uncertainty of geodynamic model predictions (Gerya et al., 2002), in sub-arc temperatures of the model geotherm (Fig 3) causes a five-fold increase in C solubility for a molecular fluid model (Connolly 2005). While electrolytic chemistry moderates this increase (Galvez et al., 2015) it is likely that such thermal effects dwarf the effect of dissolution. Thus the oft stated criticism that simple devolatilization models are incapable of explaining island arc CO_2 emissions is misplaced. The legitimate criticism of closed system models for assessing decarbonation is that the implied batch mechanism for fluid release is physically implausible.

Although the closed system model does not provide a realistic basis for assessment of slab-mantle mass transfer during subduction. Such models generally provide an upper limit for mass transfer effected without the infiltration of externally derived fluids (Kerrick and Connolly, 2001b). As such, the closed system model suggests that devolatilization processes have the potential to deplete K, H and S from subducted sediments, and almost no capacity to effect Fe or Al mass

transfer. The immobility of Al is at odds with experimental observation (e.g., Tsay et al., 2017) and may merely reflect the current limitations of the solute-species model.

4.2 Simple Back-Calculated vs Lagged Speciation

Simple back-calculated speciation (Galvez et al., 2015) assumes the mineralogy and solvent chemistry obtained by a solute-free phase equilibrium model (e.g., Fig 4b), as such the simple back-calculated model cannot account for the effects of dissolution on mineral stability. However, it is appropriate to compare the lagged and back-calculated fluid speciation to assess the accuracy of back-calculation as an approximation of fluid chemistry. This comparison (Fig 5a) is reassuring in that, at conditions within the rock-dominated regime (i.e., pressure < 6.7 GPa), the simple back-calculated speciation is generally accurate to within a factor of two or better. Thus, the only prominent disadvantage of simple back-calculation is that it provides no means of recognizing the conditions at which the assumption of a rock-dominated regime is invalid.

4.3 H2O- vs COHS-Solvent

Comparison of phase equilibria computed for the H_2O- and COHS-solvent models (Fig 4a, Fig 5b, Fig 6b) reveals only minor differences. Both models predict CO_2 as the only major C-O-H-S species (Fig 5b). Of the 25 C-O-H-S solute species considered in the H_2O-solvent model only formate ($HCOO^{2-}$) is predicted to be stable at concentrations in excess of 10^{-2} m, a prediction consistent with the observation that formate is observed as a prominent abiotic species in sea-floor hydrothermal systems (Lang et al., 2018). Although no C-O-H-S solute species were included in the COHS-solvent calculation, the use of a mixed-volatile solvent model, does not preclude the simultaneous treatment of additional molecular volatiles as solutes.

From a computational perspective the advantage of the H_2O-solvent model is that it is inexpensive and accurate in the limit of dilute molecular solute concentrations. The chief

disadvantage of the model is that it cannot be used predict phase separation, for example, the coexistence of H_2O- and CH_4- or CO_2-rich fluids (Fruh-Green et al., 2004). The availability of molecular equations for mixed-volatile solvents makes the prediction of phase separation possible; however, in practice, extrapolation of the HKF/DEW formulation to treat non-aqueous solvents is largely untested.

4.4 Open vs Closed System Devolatilization

The open system model corresponds to Rayleigh fractionation of the fluid phase. This simulates a scenario in which fluid generated by sediment devolatilization is lost immediately to the mantle wedge and that the sediments are isolated from any fluids produced at greater depth by channelized flow. The mass-loss for this model (Fig 6c) is roughly an order of magnitude below the solute mass present in the fluid for the closed system model (Fig 6a), yet the fluid speciation of both models is nearly identical (Fig 5c). Thus the difference between the models is that the open system mass-loss reflects solubilities at the time of fluid generation. That mica is refractory in the open system model demonstrates that its dehydration in the closed system model is due entirely to dissolution. As fluid generation is caused primarily by the dehydration of stilbite and lawsonite at low pressure, the open system fluid chemistry is dominated by Na and, to a lesser extent, Si and carbonate species.

The lagged fluid speciation in the closed- and open-system models is virtually identical (Fig 5c) to the pressure at which the rock-dominated limit becomes relevant for the closed system model (~6.7 GPa). The open system model does not reach this limit because the removal of Sulfur from the system stabilizes the calculation. Comparison of the open-system fluid speciation with that obtained for back-calculation (Fig 5a) illustrates that use of back-calculated results beyond the rock-dominated limit leads to substantial errors.

By excluding the possibility of fluid infiltration, the open system represents the most conservative model for subduction zone mass transfer. Based on the assumptions discussed previously in reference to the closed system model, Equation 12 yields global carbon losses by fluid fractionation (n_C = 0.05 mol/kg, Fig 6c) of 5.5 Mt/y, of which 1.1 Mt/y is lost at fore-arc depths, at the onset of fluid generation. While the uncertainties are formidable, this result suggests that indeed a simple devolatilization and dissolution process cannot explain island-arc C emissions in the range 18-55 Mt/y (Kerrick and Connolly, 2001a; Dasgupta and Hirschmann, 2010; Kelemen and Manning, 2015) and that a fluid-mediated explanation for these emissions requires that the crust be infiltrated by fluids derived by mantle dehydration.

4.5 Infiltration-Driven Devolatilization

For the subduction zone thermal model adopted here (Rupke et al., 2004), serpentine dehydration occurs top of the slab is at pressures between 3.9 and 4.6 GPa (Connolly 2005). Taking 4.3 GPa as the representative pressure and the metasediment composition obtained from the open system model at that condition (Table 1), the infiltration-driven mass transport is assessed under the assumption that the fluid released by serpentine dehydration is, and remains, pure water until it reaches the sediments. This assumption is unlikely to be true for elements such as Na and Si, which are abundant in the igneous crust, but it is a reasonable first approximation for K and C which are concentrated in the thin (~1300 m) package of altered basalt and sediment atop the subducted slab (Staudigel et al, 1989; Alt & Teagle 1999). The thinness of this package is taken as justification for reducing the problem to a zero-dimensional model. Models in which the fluid is generated within, and infiltrates through, a subducted metamorphic column are tractable (Connolly 2005; Gorman et al., 2006), but too complex for presentation here.

The initial fluid speciation in the zero-dimensional infiltration model (Fig 7b) is slightly different from the speciation for the open system model (Fig 5c) at the same pressure because the addition of pure water eliminates the small amount of diamond that is ubiquitous in the previous models and stabilizes oxidized sulfur species ($CaSO_4$, HSO_4^-, HSO_3^-). The infiltration model indicates that ~23 mol of water is required to completely decarbonate a kilogram of GLOSS metasediment (Fig 7c). As serpentinized mantle contains ~13 wt % H_2O or 7.2 mol H_2O/kg mantle, this implies a mass of serpentinite ~3.2 times that of the carbon-bearing oceanic crust is adequate to completely decarbonate the crust. The aforementioned mass is well within estimates for upper limit on the extent of mantle serpentinization (Connolly, 2005).

The elimination of mica and alkali earth elements by the addition of slightly more water than required for decarbonation leaves lawsonite as the only carrier of water at depths beyond the conditions of serpentine dehydration. With continued subduction lawsonite would dehydrate (Fig 4), leaving the metasediment completely depleted in alkali earth elements, and hydrogen and, thereby, refractory to melting. By neglecting the effect of the igneous crust on the chemistry of mantle derived fluid, the present model likely exaggerates Na-depletion. This model defect is less likely to be important for potassium, which correlates strongly with hydrogen, because of its greater solubility and lower absolute abundance in the igneous crust. Thus, the result suggests an anti-correlation between the efficacy of infiltration-driven decarbonation and slab melting. Unfortunately, there are many reasons why slab melting (Behn et al., 2011) is sporadic, and therefore its absence is not an argument for the importance of infiltration-driven decarbonation.

The complete depletion of C, K, and Na in the infiltration-driven model may seem to contradict the rock-dominated limit of the lagged speciation algorithm. This is not the case, as in the simple open-system model, because the elements depleted from the condensed phases of the system are removed with the fluid.

5. Discussion

The lagged-speciation algorithm derives extraordinary efficiency by using back-calculated fluid speciation (Galvez et al., 2015) to predict the stable composition of electrolytic fluids during Gibbs energy minimization. The cost of this efficiency is that the algorithm fails if the predicted fluid composition is inconsistent with mass balance constraints. While there is no remedy for this condition, the conditions can be recognized, making it apparent when reformulation of the solvent model or a more rigorous algorithm (e.g.: Harvie et al., 1987; Karpov et al., 2001) is required. The limitation of the algorithm related to this failing is that it cannot treat situations in which an element is present only in the form of a solute species. In the case C, O, H, and S, which appear both as molecular fluid species and common mineral constituents, this limitation can be circumvented by reformulating the solvent model to include these elements. Halogens are more problematic. There are equations of state that describe brines in terms of a solvent standard state for NaCl (Driesner and Heinrich, 2007; Aranovich et al., 2010; Dubacq et al., 2013), the complication in integrating such equations of state with solute speciation models such as the HKF is to define a relation between the macroscopic and microscopic NaCl content and to account for the resulting non-linearity in activity-composition relations. This complication has not been addressed in the current computer implementation of the lagged speciation algorithm.

In geochemical implementations of the HKF/DEW formulation water is the sole solvent and molecular volatiles and organic species are described by a solute standard state. In contrast, Galvez (2015) adopted a solvent standard state for the dominant carbonic volatile species. Both solvent formulations offer advantages in specific situations, but in the general case of a miscible water-rich solvent phase both formulations are shown here to produce comparable results (Fig 5b).

Because the primary concern of this paper is methodological, no attempt has been made to assess the accuracy of the published thermodynamic data used for the calculations presented here. This data is subject to significant random sources of error, but a bias toward under-prediction of mineral solubility is inherent in microscopic speciation models due to the existence of unanticipated species (Manning, 2007; Pokrovski and Dubrovinsky, 2011; Manning et al., 2010; Tumiati et al., 2017). Sverjensky et al. (2014) demonstrated that the current data is capable of reproducing experimental solubility data in two-component systems at subduction zone pressure conditions; however, in systems with chemistry approaching that of natural rocks, thermodynamic models underestimate the concentrations of Ca, Al, Fe, and Mg by orders of magnitude (Galvez et al. 2015). Although this error is significant, the absolute concentrations of these elements, with the probable exception of Al, is small compared to those of the alkali-earth elements at subduction zone conditions (Tsay et al., 2017).

With the aforementioned caveats, accounting for electrolytic fluids does not profoundly change assessments of the efficacy of fluid-mediated decarbonation during subduction based on classical molecular fluid models because carbonic molecular species remain prominent, if not dominant, in electrolytic fluids. The behavior of sulfur is more surprising. At fore-arc conditions S is nearly insoluble and accommodated primarily as H_2S at fore-arc conditions. The present modeling (Fig 5) suggests that sulfur solubility rises at sub-arc conditions due to the stability of oxidized sulfur species that form by the reduction of carbonate to diamond (Frezzotti et al., 2011). This rise in solubility is intriguing as a mechanism for transferring an oxygen excess to the mantle wedge.

The present models reconfirm the conclusion that sub-solidus devolatilization, as an isolated process, cannot explain extensive slab decarbonation. Gorman et al. (2006) is often cited to

support the contention that carbonate also remains in more elaborate infiltration-driven models of slab-decarbonation. However, the behavior in those models was influenced by the choice of an anomalously young slab age. Because the top of subducted slabs is heated rapidly after the slab mantle becomes detached from the lithosphere (Rupke et al., 2004), carbon-solubility rises to a maximum near sub-arc depths for typical subduction zone conditions (Connolly 2005; Fig 6 here). Slab age is important in this context because it controls when serpentine dehydration, the putative source of infiltrating fluid, is released. For subduction models based on a slab age close to the global average, there is no difficulty in explaining island-arc CO_2 emissions in terms of an infiltration-driven scenario for decarbonation (Connolly 2005; Fig 7 here). The concern over whether such models are capable of quantitatively explaining decarbonation is misplaced. Rather, the weakness of the infiltration-driven scenario is the assumption that large volumes of mantle-derived fluid equilibrates pervasively with the subducted crust. The value of incorporating electrolytic fluid chemistry in a model of the infiltration-driven devolatilization is that it offers a complete geochemical picture of the infiltration process and thereby may provide arguments for the rejection or acceptance of the mechanism. In particular, the present modeling suggests that is likely that any infiltration event capable of depleting carbon from the subducted crust would effectively desiccate the crust by potassium depletion and render the crust refractory with respect to melting.

Acknowledgements

This work was supported by Swiss National Science Foundation grant 200021_162450.

References

Ague, J.J., Nicolescu, S., 2014. Carbon dioxide released from subduction zones by fluid-mediated reactions. Nat. Geosci. 7, 355-360.

Aranovich, L.Y., Zakirov, I.V., Sretenskaya, N.G., Gerya, T.V., 2010. Ternary system H2O-CO2-NaCl at high T-P parameters: An empirical mixing model. Geochemistry International 48, 446-455.

Bebout, G.E., 1995. The impact of subduction-zone metamorphism on mantle-ocean chemical cycling. Chemical Geology 126, 191-218.

Behn, M.D., Kelemen, P.B., Hirth, G., Hacker, B.R., Massonne, H.J., 2011. Diapirs as the source of the sediment signature in arc lavas. Nat. Geosci. 4, 641-646.

Bethke, C.M., 1996. Geochemical Reaction Modeling : Concepts and Applications. Oxford University Press Inc, New York.

Canil, D., Fellows, S.A., 2017. Sulphide-sulphate stability and melting in subducted sediment and its role in arc mantle redox and chalcophile cycling in space and time. Earth and Planetary Science Letters 470, 73-86.

Chatterjee, N.D., Froese, E., 1975. A thermodynamic study of the pseudo-binary join muscovite-paragonite in the system $KAlSi_3O_8$-$NaAlSi_3O_8$-Al_2O_3-SiO_2-H_2O. American Mineralogist 60, 985-993.

Connolly, J.A.D., 2005. Computation of phase equilibria by linear programming: A tool for geodynamic modeling and its application to subduction zone decarbonation. Earth and Planetary Science Letters 236, 524-541.

Connolly, J.A.D., 2009. The geodynamic equation of state: What and how. Geochemistry Geophysics Geosystems 10.

Dasgupta, R., Hirschmann, M.M., 2010. The deep carbon cycle and melting in Earth's interior. Earth and Planetary Science Letters 298, 1-13.

Dasgupta, R., Hirschmann, M.M., Withers, A.C., 2004. Deep global cycling of carbon constrained by the solidus of anhydrous, carbonated eclogite under upper mantle conditions. Earth and Planetary Science Letters 227, 73-85.

516 DeCapitani, C., Brown, T.H., 1987. The computation of chemical equilibria in complex systems
517 containing non-ideal solutions. Geochimica Cosmochimica Acta 51, 2639-2652.
518 Driesner, T., Heinrich, C.A., 2007. The system H2O-NaCl. Part I: Correlation formulae for phase
519 relations in temperature-pressure-composition space from 0 to 1000 degrees C, 0 to 5000 bar,
520 and 0 to 1 X-NaCl. Geochimica Et Cosmochimica Acta 71, 4880-4901.
521 Dubacq, B., Bickle, M.J., Evans, K.A., 2013. An activity model for phase equilibria in the H2O-
522 CO2-NaCl system. Geochimica Et Cosmochimica Acta 110, 229-252.
523 Evans, K.A., Tomkins, A.G., Cliff, J., Fiorentini, M.L., 2014. Insights into subduction zone sulfur
524 recycling from isotopic analysis of eclogite-hosted sulfides. Chemical Geology 365, 1-19.
525 Facq, S., Daniel, I., Montagnac, G., Cardon, H., Sverjensky, D.A., 2014. In situ Raman study
526 and thermodynamic model of aqueous carbonate speciation in equilibrium with aragonite
527 under subduction zone conditions. Geochimica Et Cosmochimica Acta 132, 375-390.
528 Frezzotti, M.L., Selverstone, J., Sharp, Z.D., Compagnoni, R., 2011. Carbonate dissolution
529 during subduction revealed by diamond-bearing rocks from the Alps. Nat. Geosci. 4, 703-706.
530 Fruh-Green, G.L., Connolly, J.A.D., Plas, A., Kelley, D.S., Grobety, B., 2004. Serpentinization of
531 oceanic peridotites: Implications for geochemical cycles and biological activity, in: Wilcock,
532 W.S.D., DeLong, E.F., Kelley, D.S., Baross, J.A., Cary, S.C. (Eds.), Subseafloor Biosphere at
533 Mid-Ocean Ranges, pp. 119-136.
534 Fuhrman, M.L., Lindsley, D.H., 1988. Ternary-Feldspar Modeling and Thermometry. American
535 Mineralogist 73, 201-215.
536 Galvez, M.E., Connolly, J.A.D., Manning, C.E., 2016. Implications for metal and volatile cycles
537 from the pH of subduction zone fluids. Nature 539, 420-424.
538 Galvez, M.E., Manning, C.E., Connolly, J.A.D., Rumble, D., 2015. The solubility of rocks in
539 metamorphic fluids: A model for rock-dominated conditions to upper mantle pressure and
540 temperature. Earth and Planetary Science Letters 430, 486-498.

Gerya, T.V., Stockhert, B., Perchuk, A.L., 2002. Exhumation of high-pressure metamorphic rocks in a subduction channel: A numerical simulation. Tectonics 21.

Gorman, P.J., Kerrick, D.M., Connolly, J.A.D., 2006. Modeling open system metamorphic decarbonation of subducting slabs. Geochemistry Geophysics Geosystems 7.

Green, E.C.R., White, R.W., Diener, J.F.A., Powell, R., Holland, T.J.B., Palin, R.M., 2016. Activity-composition relations for the calculation of partial melting equilibria in metabasic rocks. Journal of Metamorphic Geology 34, 845-869.

Harvie, C.E., Greenberg, J.P., Weare, J.H., 1987. A chemical-equilibrium algorithm for highly nonideal multiphase systems - free-energy minimization. Geochimica Et Cosmochimica Acta 51, 1045-1057.

Holland, T.J.B., Powell, R., 1998. An internally consistent thermodynamic data set for phases of petrological interest. Journal of Metamorphic Geology 16, 309-343.

Jennings, E.S., Holland, T.J.B., 2015. A Simple Thermodynamic Model for Melting of Peridotite in the System NCFMASOCr. Journal of Petrology 56, 869-892.

Kagoshima, T., Sano, Y., Takahata, N., Maruoka, T., Fischer, T.P., Hattori, K., 2015. Sulphur geodynamic cycle. Scientific Reports 5.

Karpov, I.K., Chudnenko, K.V., Kulik, D.A., Avchenko, O.V., Bychinskii, V.A., 2001. Minimization of gibbs free energy in geochemical systems by convex programming. Geochemistry International 39, 1108-1119.

Kelemen, P.B., Manning, C.E., 2015. Reevaluating carbon fluxes in subduction zones, what goes down, mostly comes up. Proceedings of the National Academy of Sciences of the United States of America 112, E3997-E4006.

Kerrick, D.M., Connolly, J.A.D., 2001a. Metamorphic devolatilization of subducted marine sediments and the transport of volatiles into the Earth's mantle. Nature 411, 293-296.

Kerrick, D.M., Connolly, J.A.D., 2001b. Metamorphic devolatilization of subducted oceanic metabasalts: implications for seismicity, arc magmatism and volatile recycling. Earth and Planetary Science Letters 189, 19-29.

Lang, S.Q., Fruh-Green, G.L., Bernasconi, S.M., Brazelton, W.J., Schrenk, M.O., McGonigle, J.M., 2018. Deeply-sourced formate fuels sulfate reducers but not methanogens at Lost City hydrothermal field. Scientific Reports 8.

Leal, A.M.M., Kulik, D.A., Smith, W.R., Saar, M.O., 2017. An overview of computational methods for chemical equilibrium and kinetic calculations for geochemical and reactive transport modeling. Pure and Applied Chemistry 89, 597-643.

Manning, C.E., Antignano, A., Lin, H.A., 2010. Premelting polymerization of crustal and mantle fluids, as indicated by the solubility of albite plus paragonite plus quartz in H2O at 1 GPa and 350-620 degrees C. Earth and Planetary Science Letters 292, 325-336.

Manning, C.E., Shock, E.L., Sverjensky, D.A., 2013. The Chemistry of Carbon in Aqueous Fluids at Crustal and Upper-Mantle Conditions: Experimental and Theoretical Constraints, in: Hazen, R.M., Jones, A.P., Baross, J.A. (Eds.), Carbon in Earth, pp. 109-148.

Mason, E., Edmonds, M., Turchyn, A.V., 2017. Remobilization of crustal carbon may dominate volcanic arc emissions. Science 357.

Plank, T., Langmuir, C.H., 1998. The chemical composition of subducting sediment and its consequences for the crust and mantle. Chemical Geology 145, 325-394.

Pokrovski, G.S., Dubrovinsky, L.S., 2011. The S-3(-) Ion Is Stable in Geological Fluids at Elevated Temperatures and Pressures. Science 331, 1052-1054.

Poli, S., 2015. Carbon mobilized at shallow depths in subduction zones by carbonatitic liquids. Nat. Geosci. 8, 633-+.

Prausnitz, J.M., 1969. Molecular thermodynamics of fluid-phase equilibria. Prentice-Hall, Englewood Cliffs, NJ.

590 Rupke, L.H., Morgan, J.P., Hort, M., Connolly, J.A.D., 2004. Serpentine and the subduction
591 zone water cycle. Earth and Planetary Science Letters 223, 17-34.
592 Shock, E.L., Helgeson, H.C., 1988. Calculation of the thermodynamic and transport-properties
593 of aqueous species at high-pressures and temperatures - correlation algorithms for ionic
594 species and equation of state predictions to 5-kb and 1000-degrees-c. Geochimica Et
595 Cosmochimica Acta 52, 2009-2036.
596 Skora, S., Blundy, J.D., Brooker, R.A., Green, E.C.R., de Hoog, J.C.M., Connolly, J.A.D., 2015.
597 Hydrous Phase Relations and Trace Element Partitioning Behaviour in Calcareous Sediments
598 at Subduction-Zone Conditions. Journal of Petrology 56, 953-980.
599 Stern, R.J., 2002. Subduction zones. Reviews of Geophysics 40.
600 Sverjensky, D.A., Harrison, B., Azzolini, D., 2014. Water in the deep Earth: The dielectric
601 constant and the solubilities of quartz and corundum to 60 kb and 1200 degrees C.
602 Geochimica Et Cosmochimica Acta 129, 125-145.
603 Sverjensky, D.A., Huang, F., 2015. Diamond formation due to a pH drop during fluid-rock
604 interactions. Nature Communications 6.
605 Tsay, A., Zajacz, Z., Ulmer, P., Sanchez-Valle, C., 2017. Mobility of major and trace elements in
606 the eclogite-fluid system and element fluxes upon slab dehydration. Geochimica Et
607 Cosmochimica Acta 198, 70-91.
608 Tumiati, S., Tiraboschi, C., Sverjensky, D.A., Pettke, T., Recchia, S., Ulmer, P., Miozzi, F., Poli,
609 S., 2017. Silicate dissolution boosts the CO2 concentrations in subduction fluids. Nature
610 Communications 8.
611 Wolery, T.J., 1992. A Software Package for Geochemical Modeling of Aqueous Systems:
612 Package Overview and Installation Guide. Lawrence Livermore National Laboratory,
613 Livermore, California.
614

Figure Captions

Fig 1. Schematic specific Gibbs energy (g) vs composition (x_{SiO2}) diagram for the H_2O-SiO_2 system illustrating conditions for failure of the lagged speciation algorithm as discussed in the text.

Fig 2. True (a) and algorithmic representation (b) of phase relations in the $CaSiO_3$-SiO_2-H_2O system with a one-component solvent (H_2O), wollastonite, quartz, and fluid as possible phases illustrating conditions for failure of the lagged speciation algorithm as discussed in the text.

Fig 3. Geotherm assumed for the subduction zone models (Ruepke et al. 2004).

Fig 4. Volumetric phase proportions during closed-system devolatilization of the GLOSS sediment composition (Table 1) computed by (a) lagged speciation and (b) without taking into account dissolution. The lagged speciation results compare the COHS-solvent model (solid curves) and the H_2O-solvent model (dashed curves) commonly assumed in applications of the DEW/HKF formalism. The fields for small amounts of graphite, potassium feldspar, clinoamphibole, and pumpellyite, which are stable at low pressure, are not labelled. Mineral proportions (not shown) computed for the open-system devolatilization model are essentially identical to those obtained by neglecting dissolution. Phase notation and solution models are summarized in Table 2.

Fig 5. Fluid speciation in various models for the devolatilization of the GLOSS sediment composition. (a) Closed-system devolatilization with the COHS-solvent model, comparing the lagged (solid curves) and simple back-calculated (dashed curves) speciation. (b) Closed-system devolatilization using lagged speciation, comparing the COHS- (solid curves) and H_2O-solvent

(dashed curves) models. (c) COHS-solvent using lagged speciation, comparing open- (diamond symbols) and closed-system (solid curves) devolatilization. In simple back-calculation, fluid speciation is calculated post-hoc from the solute-free phase equilibrium model (Fig 4b), thus the phase proportions and fluid composition violate mass balance. Nonetheless, the back-calculated speciation is accurate to within a factor of two within the rock-dominated limit (i.e., at pressure < ~6.7 GPa).

Fig 6. Mass present in, or removed by, the fluid generated during devolatilization of 1 kg of GLOSS sediment in various models. (a) Closed system: COHS-solvent, lagged speciation (solid curves) vs COHS molecular fluid (dashed curve for C). (b) Closed system, lagged speciation: COHS-solvent (solid curves) vs H_2O-solvent (dashed curves). (c) Open system: COHS-solvent (diamond symbols) vs COHS molecular fluid (circular symbols for C); symbols indicate the points along the subduction path at which fluid was generated. In closed system models, the mass of a component present in the fluid may decrease with pressure due to changing solubility; in the open system model, mass loss is irreversible.

Fig 7. Phase proportions (a), fluid speciation (b), and mass loss (c) for the infiltration-driven devolatilization model. Phase notation and solution models are summarized in Table 2.

Tables

Table 1. Average subducted sediment composition (GLOSS, Plank and Langmuir, 1989). The GLOSS composition has been modified by the addition of sulfur corresponding to the presence of ~0.1 volume % pyrite, the original O_2 content has been recomputed so that the bulk composition is redox neutral. The metasediment composition is the bulk composition obtained at 4.3 GPa from the GLOSS composition by open-system devolatilization (Fig 6c).

	Initial GLOSS Sediment		Metasediment at 4.3 GPa	
	mass fraction, %	mol/kg	mass fraction, %	mol/kg
H_2	0.823	4.085	0.197	0.978
C	0.824	0.686	0.847	0.706
Si	27.621	9.835	29.317	10.439
Al	6.369	2.360	6.802	2.521
Fe	4.112	0.736	4.392	0.786
Mg	1.520	0.625	1.623	0.668
Ca	4.285	1.069	4.551	1.135
Na	1.809	0.787	1.804	0.785
K	1.735	0.444	1.798	0.460
O_2	50.578	15.806	48.322	15.101
S_2	0.323	0.101	0.345	0.108

667 Table 2. Mineral notation, formulae and solution model sources (1 - Green et al., 2016; 2 -
668 Holland and Powell, 1998; 3 - Fuhrman and Lindsley, 1988; 4 - Jennings and Holland, 2015; 5 -
669 Chatterjee and Froese, 1975). See Appendix for condensed phase and fluid species
670 thermodynamic data sources.

671

Symbol	Solution	Formula	Source
Amph	clinoamphibole	$Ca_{2(y+u+v)}Na_{u+2(w+z)}[Mg_xFe_{1-x}]_{7-3u-2v-4(w+z)}Fe_{2z}Al_{4y+3v+2w}Si_{8-(y+v)}O_{22}(OH)_2$	1
arag	aragonite	$CaCO_3$	
cc	calcite	$CaCO_3$	
coe	coesite	SiO_2	
Cpx	clinopyroxene	$Na_{y+w}[CaMg_xFe_{1-x}]_{1-y-w}Al_yFe_wSi_2O_6$	1
Dol	dolomite	$CaMg_xFe_{1-x}(CO_3)_2$	2
F	fluid		
Fsp	feldspar	$K_yNa_xCa_{1-x-y}Al_{2-x-y}Si_{2+x+y}O_8$	3
Grt	Garnet	$[Fe_xCa_yMg_{1-x-y}]_3[Fe_{1-v}Al_v]_2Si_3O_{12}$	4
ky	kyanite	Al_2SiO_5	
law	lawsonite	$CaAl_2Si_2O_6(OH)_2$	
M	magnesite	$Mg_xFe_{1-x}CO_3$	2
Ms	muscovite	$K_xNa_{1-x}[Mg_{1-v}Fe_v]_yAl_{3-y}Si_{3+y}O_{10}(OH)_2$	5
Pu	pumpellyite	$Ca_4Mg_xFe_{1-x}[Fe_yAl_{1-y}]_5Si_6O_{21}(OH)_7$	ideal
q	quartz	SiO_2	
stlb	stilbite	$CaAl_2Si_7O_{11}(OH)_{14}$	
Stlp	stilpnomelane	$K_{0.5}[Mg_{1-x}Fe_x]_5Al_2Si_8O_{18}(OH)_{12.5}$	ideal
stv	stishovite	SiO_2	

672

Graphical Abstract (for review)

Computed phase changes, fluid speciation, and mass loss as a function of water infiltration through metasediment at sub-arc conditions.

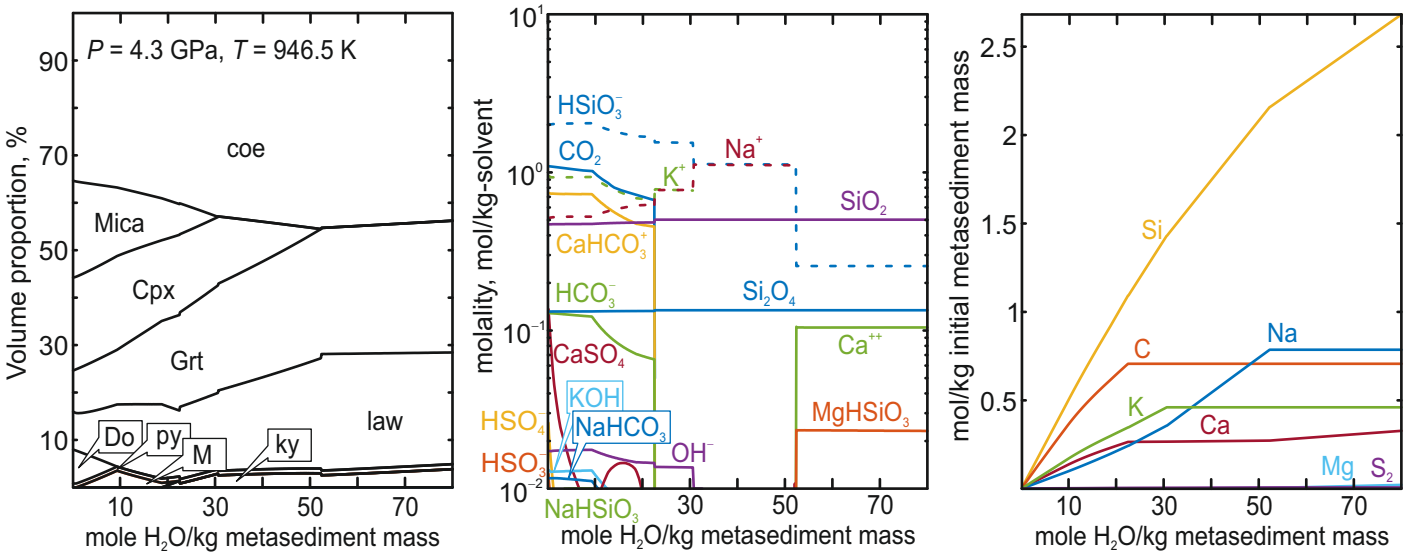

Figure
Click here to download Figure: Figures_Connolly.pdf

Figure 1

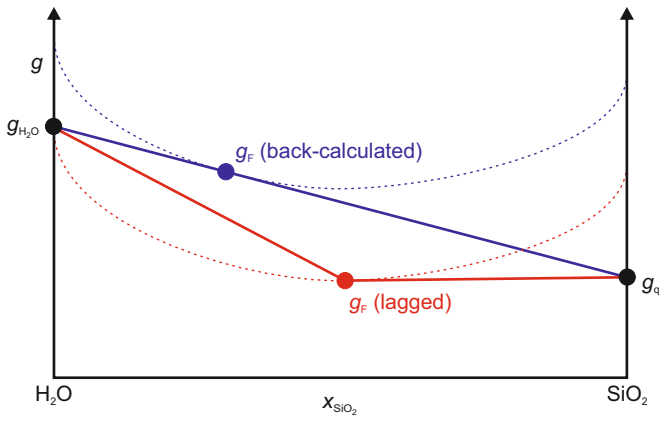

Figure 2

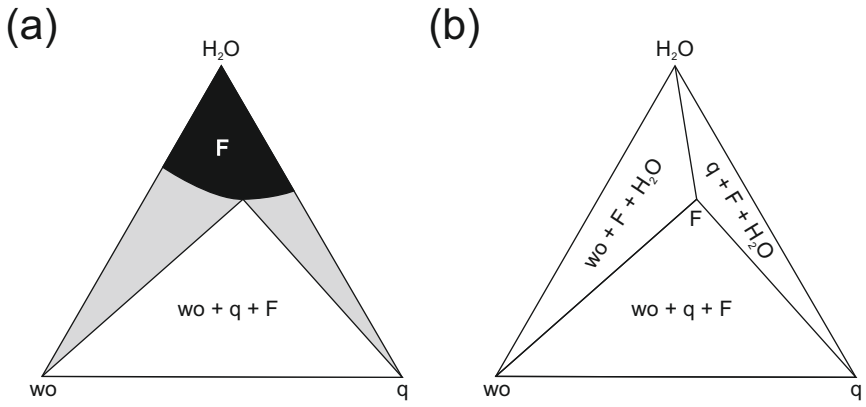

Figure 3

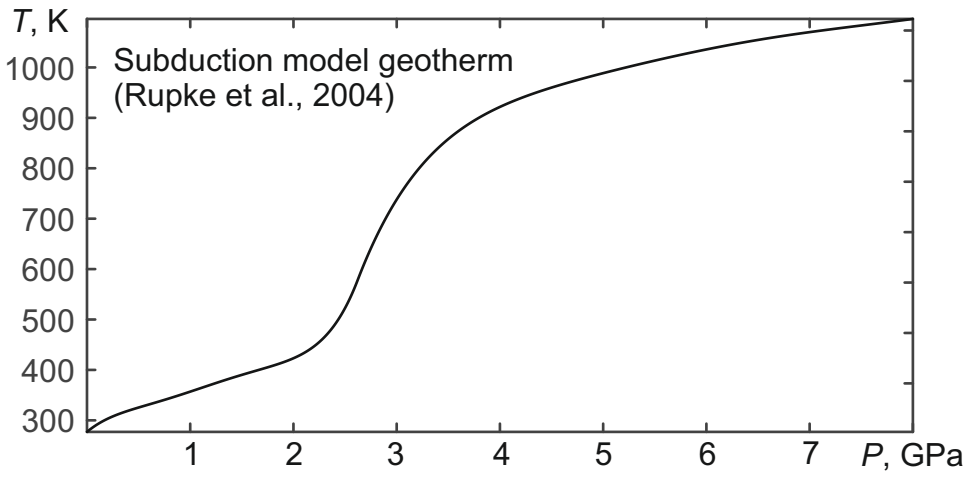
T, K
1000
900
800
700
600
500
400
300
Subduction model geotherm
(Rupke et al., 2004)
1
2
3
4
5
6
7
P, GPa

Figure 4

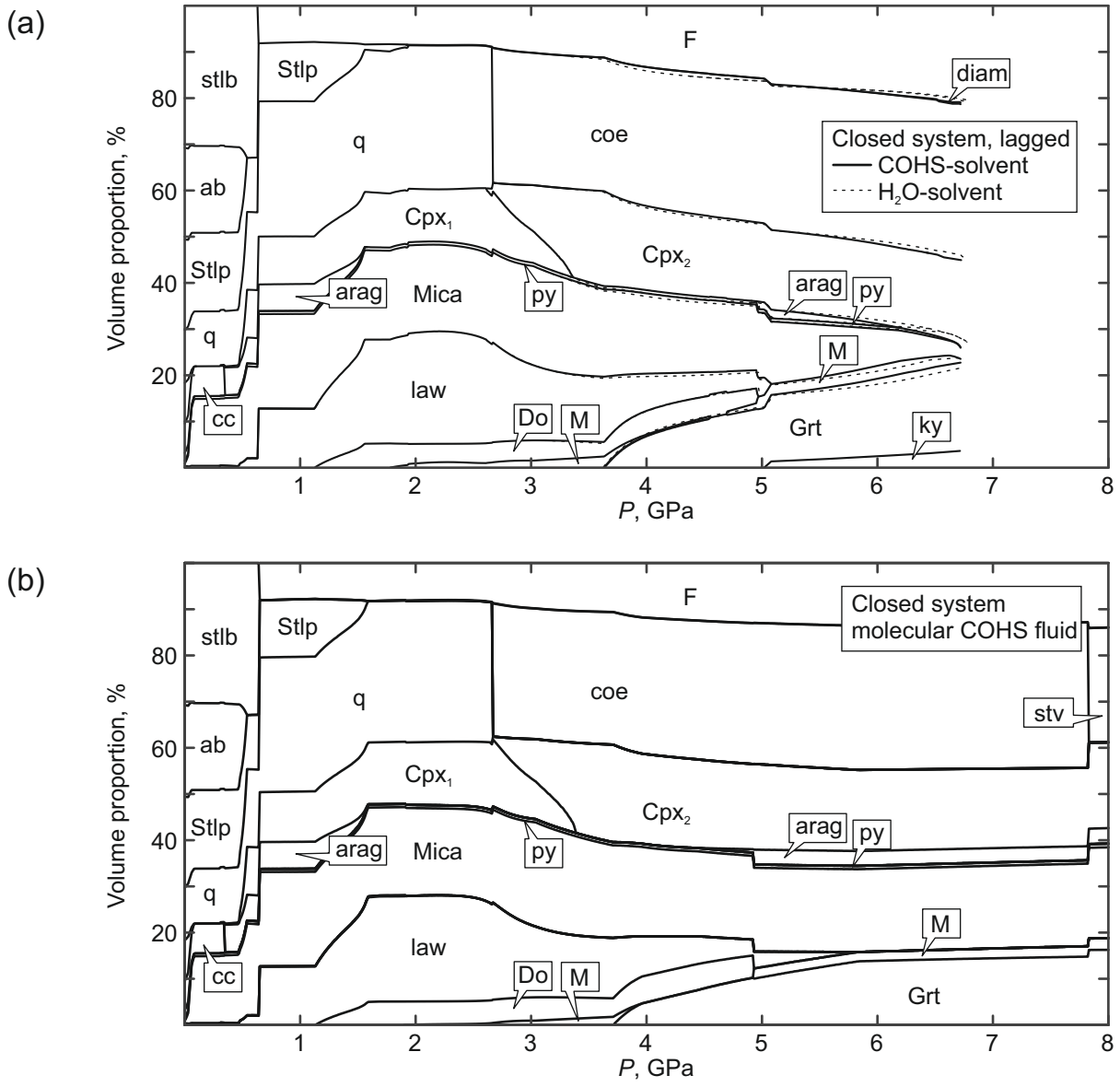
(a)
Volume proportion, %
P, GPa
stlb
Stlp
F
diam
q
coe
Closed system, lagged
COHS-solvent
H2O-solvent
ab
Cpx1
Cpx2
Stlp
arag
Mica
py
arag
py
q
M
law
cc
Do
M
Grt
ky
(b)
Volume proportion, %
P, GPa
stlb
Stlp
F
Closed system
molecular COHS fluid
q
coe
stv
ab
Cpx1
Cpx2
Stlp
arag
Mica
py
arag
py
q
M
law
cc
Do
M
Grt

Figure 5

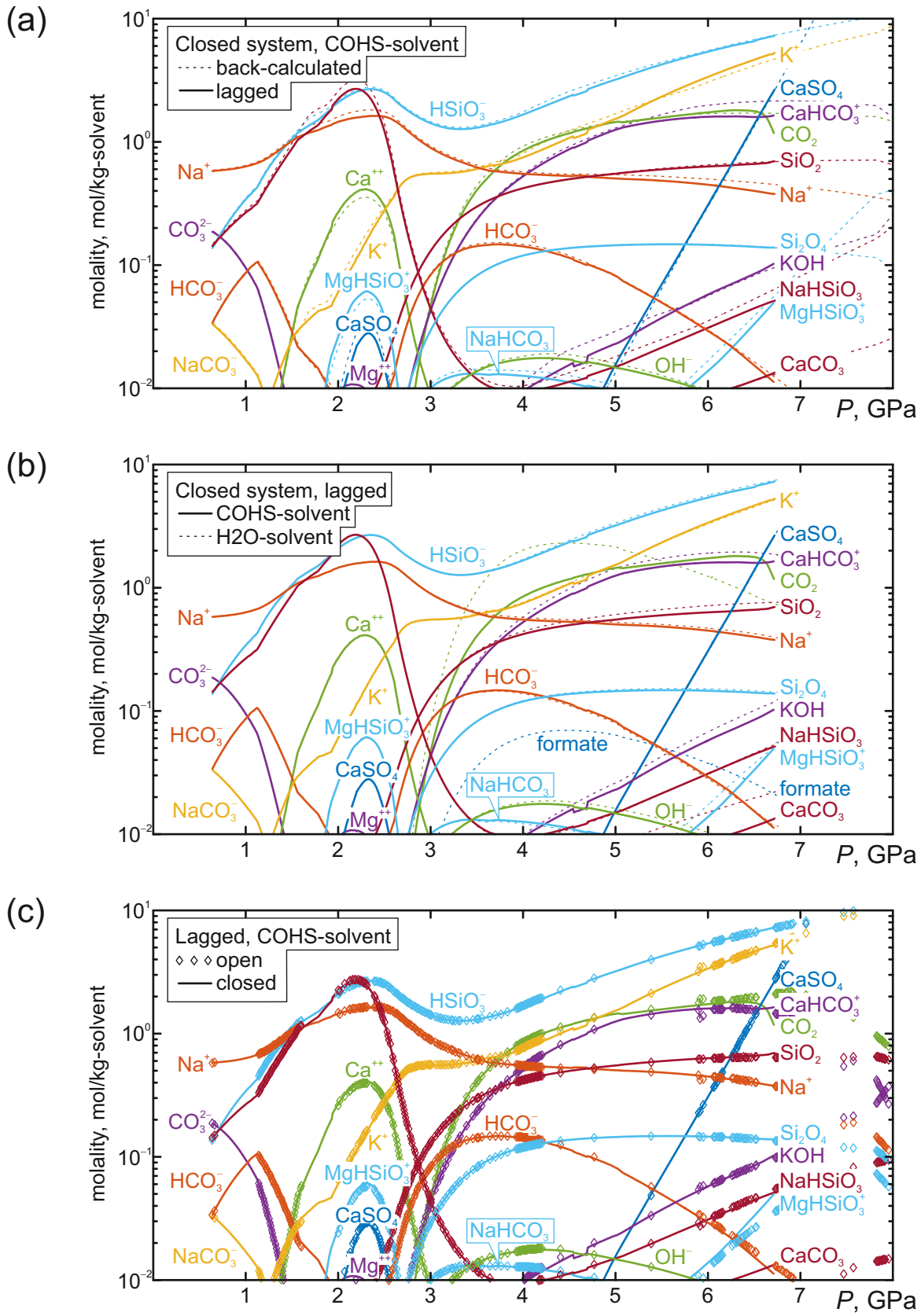
(a)
Closed system, COHS-solvent
back-calculated
lagged
molality, mol/kg-solvent
P, GPa
(b)
Closed system, lagged
COHS-solvent
H2O-solvent
molality, mol/kg-solvent
P, GPa
(c)
Lagged, COHS-solvent
open
closed
molality, mol/kg-solvent
P, GPa
HSiO3-
Na+
CO3 2-
HCO3-
NaCO3-
Ca++
K+
MgHSiO3+
CaSO4
Mg++
NaHCO3
OH-
formate
K+
CaSO4
CaHCO3+
CO2
SiO2
Na+
Si2O4
KOH
NaHSiO3
MgHSiO3+
CaCO3

Figure 6

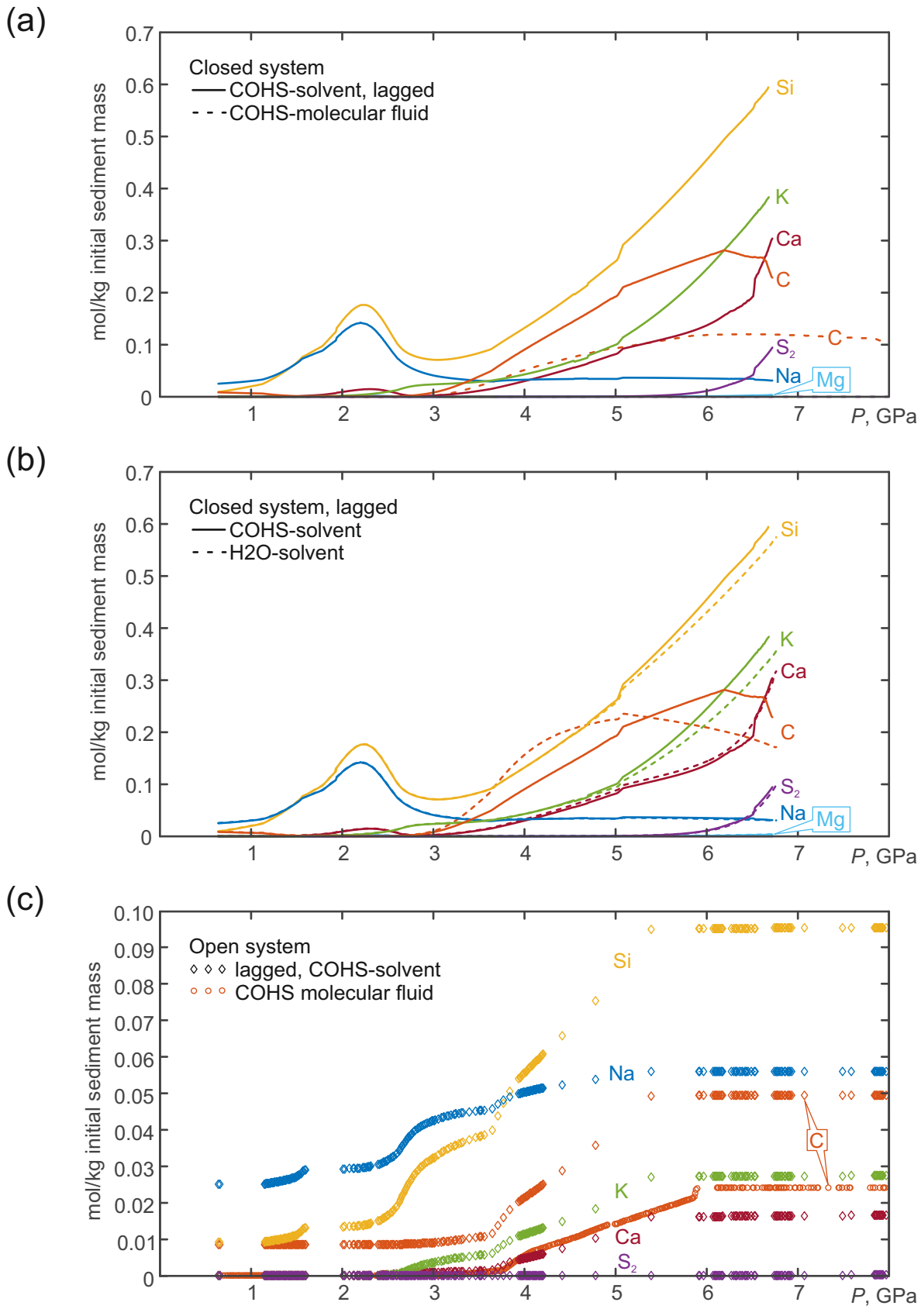
(a)
Closed system
COHS-solvent, lagged
COHS-molecular fluid
mol/kg initial sediment mass
P, GPa
Si
K
Ca
C
C
S2
Na
Mg
(b)
Closed system, lagged
COHS-solvent
H2O-solvent
mol/kg initial sediment mass
P, GPa
Si
K
Ca
C
S2
Na
Mg
(c)
Open system
lagged, COHS-solvent
COHS molecular fluid
mol/kg initial sediment mass
P, GPa
Si
Na
C
K
Ca
S2

Figure 7

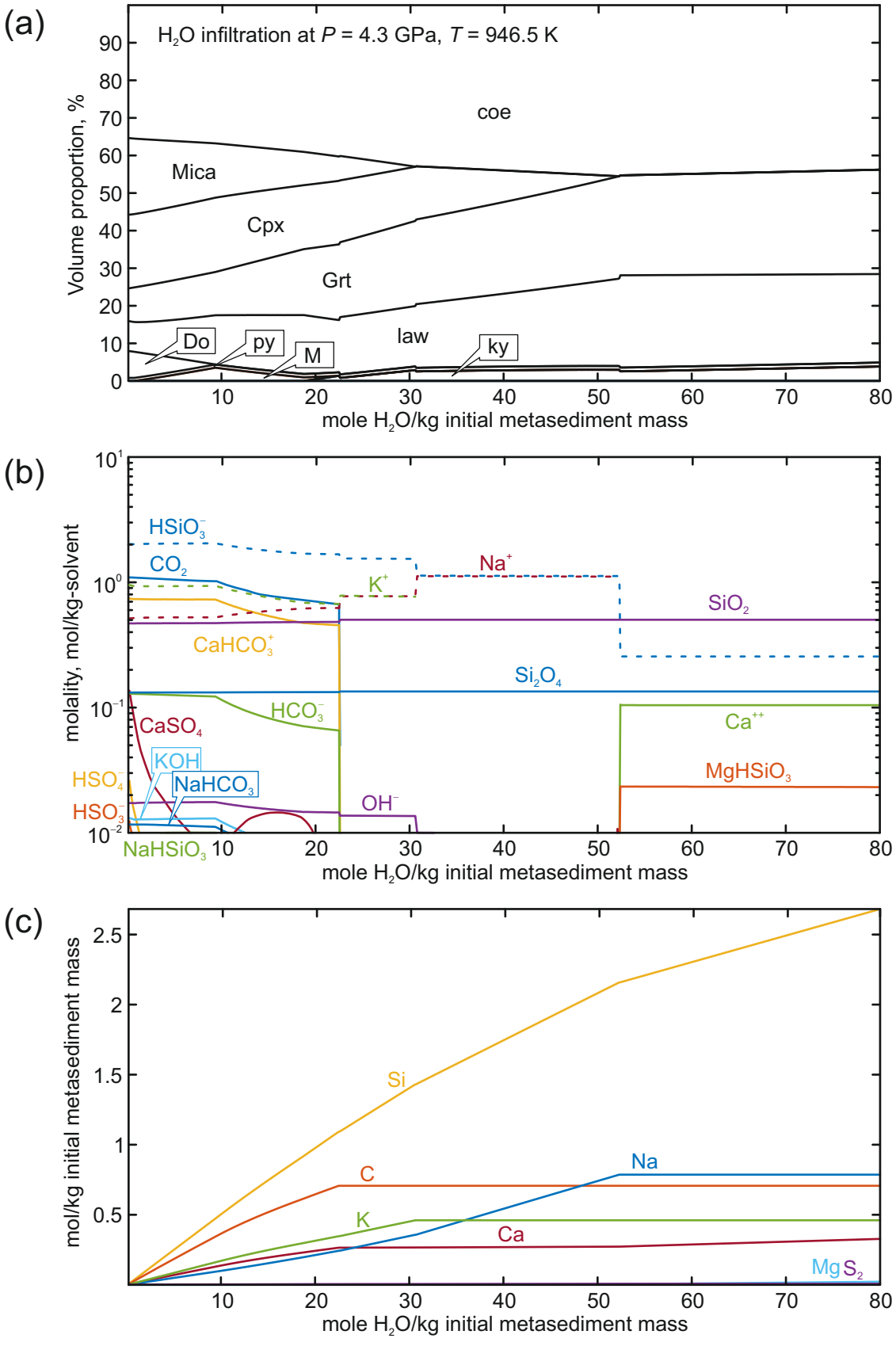
(a)
H2O infiltration at P = 4.3 GPa, T = 946.5 K
coe
Mica
Cpx
Grt
law
Do
py
M
ky
Volume proportion, %
mole H2O/kg initial metasediment mass
(b)
HSiO3−
CO2
K+
Na+
SiO2
CaHCO3+
Si2O4
HCO3−
CaSO4
Ca++
KOH
NaHCO3
MgHSiO3
HSO4−
HSO3−
OH−
NaHSiO3
molality, mol/kg-solvent
mole H2O/kg initial metasediment mass
(c)
Si
C
Na
K
Ca
Mg
S2
mol/kg initial metasediment mass
mole H2O/kg initial metasediment mass

Supplementary material for online publication only

Click here to download Supplementary material for online publication only: SOM_Connolly.pdf